Electrochimica Acta 254 (2017) 328–336

Contents lists available at ScienceDirect

Electrochimica Acta

journal homepage: www.elsevier.com/locate/electacta

Monolithic Hierarchical Carbon Assemblies Embedded with Mesoporous $NaTi_2(PO_4)_3$ Nanocrystals for Flexible High-Performance Sodium Anodes

Guobao Xu[a], Zhongyu Li[a], Xiaolin Wei[a], Liwen Yang[a,*], Paul K. Chu[b]

[a] Hunan Key Laboratory of Micro-Nano Energy Materials and Devices, School of Physics and Optoelectronics, Xiangtan University, Hunan 411105, China
[b] Department of Physics and Materials Science, City University of Hong Kong, Tat Chee Avenue, Kowloon, Hong Kong, China

ARTICLE INFO

Article history:
Received 13 May 2017
Received in revised form 17 September 2017
Accepted 19 September 2017
Available online 22 September 2017

Keywords:
Sodium-ion batteries
Hetero-assembly
Monolithic
Mesoporous nanocrystals
Graphene
Carbon nanotubes

ABSTRACT

Monolithic hierarchical porous carbon assemblies embedded with mesoporous $NaTi_2(PO_4)_3$ nanocrystals suitable for flexible anodes in sodium ion batteries (SIBs) are prepared by modified vacuum filtration and annealing. The fabrication involves two-step hetero-assembly induced by electrostatic interactions. In the hierarchical porous carbon assembly, the ultrathin amorphous carbon layers connect the mesoporous $NaTi_2(PO_4)_3$ nanocrystals with the 3D interconnected carbon networks of reduced graphene oxide and carbon nanotubes. Owing to the synergistic effects rendered by the mesoporous nanocrystals and hierarchical porous carbon networks, the unique monolithic assembly provides continuous 3D pathways for electron/ion conduction and enhances the structural stability during repetitive Na insertion/extraction. As a flexible anode in SIBs, it delivers outstanding room-temperature electrochemical performance with high reversible capacity (125 $mAhg^{-1}$ at 1 C), long cycling life (82% capacity retention after 5,000 cycles at 10 C), as well as high rate capability (73 $mAhg^{-1}$ at 30 C). The flexible monolithic anode which exhibits high Coulombic efficiency and reversible capacity at 0 °C and 50 °C has large potential in flexible high-performance SIBs.

1. Introduction

Flexible energy storage systems have attracted much attention due to promising applications in smart electronics, wearable devices, and rollup displays [1–3] and flexible Li-ion batteries are important power sources for these electronic devices because of the large energy density and power density as well as long cycling life. However, future large-scale applications are prone to increasing costs and limited natural resource of lithium. Consequently, flexible sodium ion batteries (SIBs) with similar working principles as LIBs are receiving increasing attention as a good alternative because of the large natural abundance, low cost, and availability of sodium [4–7]. The design and fabrication of reliable flexible anodes with high capacity, high rate capability, and long-term stability are crucial to the development of high-performance SIBs for flexible electronic devices [8,9].

Owing to the larger ionic radius of sodium ions and strong binding in rigid inorganic lattices, it is challenging to develop suitable Na-host materials to meet requirements for SIBs applications in terms of safety, power capability, and cycling life. Recently, Na-superionic conductor (NASICON) compounds have been investigated as potential electrode materials in high-performance SIBs due to the open framework containing large interstitial channels which can provide high ionic mobility [10]. Among these compounds, $NaTi_2(PO_4)_3$ (NTP) is a promising anode material in SIBs on account of 3D NASICON frameworks with long-term cycling stability, high ion conductivity for good rate capability, large theoretical capacity (133 $mAhg^{-1}$), low cost and safety [11,12]. However, practical application of NTP to high-performance SIBs is hampered by the poor cycling ability and inferior rate performance as a result of the low electron conductivity and sluggish charge transfer kinetics. To overcome the hurdle, the electrochemical performance of NTP can be enhanced by using nano-NTP particles and hybridization with conductive additives [13–20]. For example, Yang et al. synthesized carbon and TiO_2 coated NTP nanocube composites which showed high rate capability (83.5 $mAhg^{-1}$ at ~10C) and long-term cyclability [17]. There has been increasing effort to improve the electron/ion transport kinetics of the NTP by embedding the micro/nano-structured NTP in highly conductive 3D carbon frameworks

* Corresponding author.
E-mail address: ylwxtu@xtu.edu.cn (L. Yang).

http://dx.doi.org/10.1016/j.electacta.2017.09.121
0013-4686/

such as graphene, carbon nanotubes and their combination [21–25]. In these composites, the former provides abundant active sites and short distance for ion and electron transport, while the latter provides the 3D electronic pathways among NTP particles to increase conductivity and also serves as a robust and flexible buffer to accommodate the volume change during repetitive Na insertion/extraction during cycling. The synergistic coupling between each constituent often produces an abnormal surface/interface Na storage behavior. Wu et al. prepared a nanocomposite comprising porous NTP nanocrystals embedded in a 3D graphene network with high rate capability of 67 $mAhg^{-1}$ at 50 C, 80% capacity retention after 1,000 cycles at 10C, and high initial Coulombic efficiency of 79% [21]. Fang et al. prepared 3D graphene decorated NTP microspheres with high reversible capacity (130 $mAhg^{-1}$ at 0.1 C), long cycling life (77% capacity retention after 1,000 cycles at 20C) and high rate capability (38 $mAhg^{-1}$ at 200 C) [22]. However, despite recent advances, free-standing and flexible electrodes consisting of micro/nano-structured NTP and 3D highly-conductive hierarchical carbon frameworks with outstanding rate performance, ultra-long cycle life and high capacity are still difficult to realize.

Herein, we report the preparation of monolithic hierarchical porous carbon assembly embedded with 73 wt% mesoporous NTP (MNTP) nanocrystals (designated as C-MNTP⊂rGO-CNTs) by a modified vacuum filtration process followed by annealing. In the hierarchical porous carbon assembly, the ultrathin amorphous carbon layers bridge the MNTP nanocrystals with 3D interconnected networks of rGO and CNTs. Incorporation of CNTs into the monolithic assemblies suppresses re-stacking of graphene, provides robust and well-interconnected conductive pathways in the electrode matrix to facilitate charge transfer and enhance reaction kinetics, and ensures better mechanical properties than a single component. The monolithic C-MNTP⊂rGO-CNTs assemblies are excellent flexible anodes in SIBs by delivering outstanding room-temperature (RT) electrochemical performance such as high reversible capacity (125 $mAhg^{-1}$ at 1 C), long cycling life (82% capacity retention after 5,000 cycles at 10 C), and high rate capability (73 $mAhg^{-1}$ at 30 C). The flexible monolithic anode also has high Coulombic efficiency and reversible capacity at both 0 °C and 50 °C.

2. Experimental Details

2.1. Synthesis of MNTP nanocrystals

The crystalline MNTP nanocrystals were prepared by a simple solvent-thermal reaction followed by annealing at 600 °C and more details about the fabrication process can be found in our previous paper [26]. Briefly speaking, 40 mL of ethanol with 2 mmol titanium (IV) butoxide (0.68 ml) and 6 mL of phosphoric acid (85 wt%) with 2 mmol CH_3COONa(0.164 g) were mixed and stirred for 0.5 h. The solution was transferred to a Teflon vessel and kept at 160 °C for 3 h. The white powder was collected by centrifugation, washed, dried, and annealed at 600C for 2 h to obtain the MNTP nanocrystals.

2.2. Fabrication of monolithic C-MNTP⊂rGO-CNTs assemblies

The monolithic C-MNTP⊂rGO-CNTs assemblies were fabricated by a modified vacuum filtration process and subsequent annealing. The crystalline MNTP nanocrystals (about 80 mg) were dispersed into a bovine serum albumin (BSA) solution (0.5 wt%) under stirring and after an ultrasonic treatment for 2 h at room temperature, the BSA-coated MNTP nanocrystals were collected by centrifugation. The BSA-coated MNTP nanocrystals were re-dispersed in the NH_4HCO_3 solution (1 mg/mL), and a suitable amount of solution with oxidized CNTs (0.5 mg/mL) was added dropwise under continuous stirring. The homogeneous intermediate of the CNTs and BSA-coated MNTP nanocrystals was produced in ten minutes by exploiting the electrostatic interactions between them. The intermediate composed of CNTs and BSA-coated MNTP nanocrystals was added dropwise to the solution with graphene oxide (GO, 1 mg/mL) under magnetic stirring. Owing to the electrostatic interactions between the GO sheets and intermediate of oxidized CNTs and BSA-coated MNTP nanocrystals, the foam-like composite was formed on the bottom in ten minutes after the stirring ceased. The foam-like composite was collected by vacuum filtration using a microporous membrane with a pore size of 0.45 μm. The peeled samples were dried at 60 °C for 6 h and further annealed under Ar/H_2 (5%) at 600 °C for 2 h to obtain the monolithic C-MNTP⊂rGO-CNTs assemblies. The thickness of the monolithic C-MNTP⊂rGO-CNTs assemblies was controlled by adjusting the amount of the fluffy composite. For comparison, monolithic assemblies consisting of similar contents of MNTP nanocrystals and rGO (or CNTs) (designated as C-MNTP⊂rGO or C-MNTP⊂CNT) were prepared by the same procedures but without electrostatic assembly of the oxidized CNTs (or GO) and BSA-coated MNTP nanocrystals.

2.3. Materials characterization

The crystal structure of the samples was determined by X-ray diffraction (XRD, Rigaku D/max 2500) and Raman scattering was conducted on a Renishaw inVia system with the 532 nm laser as a excitation source. The morphology and microstructure were characterized by scanning electron microscopy (SEM) and transmission electron microscopy (TEM, JEOL 2100F) equipped with selected-area electron diffraction (SAED) and Oxford energy-dispersive X-ray spectroscopy (EDS). The amount of MNTP nanocrystals was determined by thermal gravimetric analysis

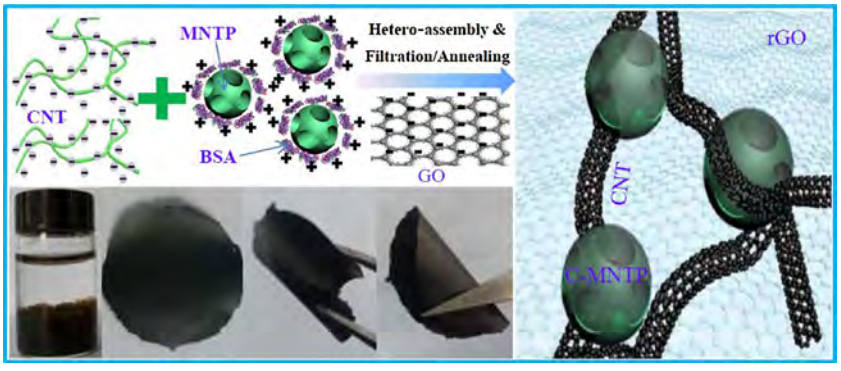

Fig. 1. Schematic of the fabrication procedures and digital images of the macroscopically visible assembled intermediate and monolithic C-MNTP⊂rGO-CNTs electrodes.

(TGA) and differential scanning calorimetry (DSC) performed on a TGA 2050 thermo gravimetric analyzer. X-ray photoelectron spectroscopy (XPS) was carried out using an Al K_α source (Kratos Analytical Ltd., UK) and the binding energy of 284.8 eV for C 1 s was used as calibration. The nitrogen adsorption–desorption isotherms were obtained at 77 K (Quantachrome NOVA 4000e).

2.4. Electrochemical characterization

The self-supporting monolithic C-MNTP⊂rGO-CNTs and C-MNTP⊂rGO assemblies without any other conductive carbon and binders were directly used as working electrodes in electrochemical characterizations. The control MNTP electrode was prepared by mixing the prepared NCs, super P carbon black and the PVDF binder at a weight ratio of 70: 20: 10 with subsequent coating on Cu collectors. The CR2032-type coin cells were assembled in an argon-filled glove box with water and oxygen concentrations below 1 ppm with metallic sodium foil as the counter electrodes and glass fibers (Whatman GF/D) as the separators. The electrolyte was 1 M $NaClO_4$ in a 1:1 (volume) mixture of ethylene carbonate/propylene carbonate. The galvanostatic charging–discharging (GCD) profiles were acquired at different current densities in a voltage range between 1.5 and 3 V (vs. Na/Na^+) on a NEWARE BTS-610 multi-channel battery testing system. Cyclic voltammetry (CV) was performed on the CHI660E (Chenhua, Shanghai) electrochemical workstation in a voltage range between 1.5 and 3 V (vs. Na/Na^+) at different scanning rates. Electrochemical impedance spectroscopy (EIS) was conducted on the CHI660E (Chenhua, Shanghai) electrochemical workstation by applying a perturbation voltage of 5 mV in a frequency range of 10^5 to 10^{-2} Hz.

3. Results and discussion

As shown in Fig. 1, the monolithic C-MNTP⊂rGO-CNTs electrodes are fabricated by a modified vacuum filtration process and annealing. In our experiments, we paid more attention to the following two factors. One is the flexibility and self-supporting feature. According to our previous studies [27], in order to obtain good flexibility and self-supporting feature, it is better for the content of RGO to be beyond 20%. The other is the content of MNTP nanocrystals. The high ratio of MNTP nanocrystals in the electrode is very important for the practical application. On the other hand, the contents of NTP active materials in reported literatures using slurry-coating process in the traditional electrode configuration were about 70%. To obtain high content of MNTP nanocrystals for comparison with the reported results, the content of about 70% MNTP nanocrystals was selected. Based on above-mentioned consideration, the nominal ratio of 25:5:70 for GO, CNTs and MNTP was considered. The synthesis involves a two-step hetero-assembly induced by electrostatic interactions. In our previous study, owing to the abundant —OH groups on the surface, crystalline MNTP nanocrystals with a diameter of about 100 nm and pore size between 1 and 10 nm were grafted with BSA molecules *via* strong hydrophilic interactions by using a simple dipping process [23,28]. Here, in the solution containing NH_4HCO_3, the BSA-grafted MNTP nanocrystals are positively charged, whereas the CNTs oxidized by nitric acid are negatively charged. Owing to the electrostatic interactions, a small quantity of oxidized CNTs is dispersed in the surrounding BSA-grafted MNTP nanocrystals by hetero-assembly to produce the positively charged hybrid. The GO sheets prepared by the modified Hummers method

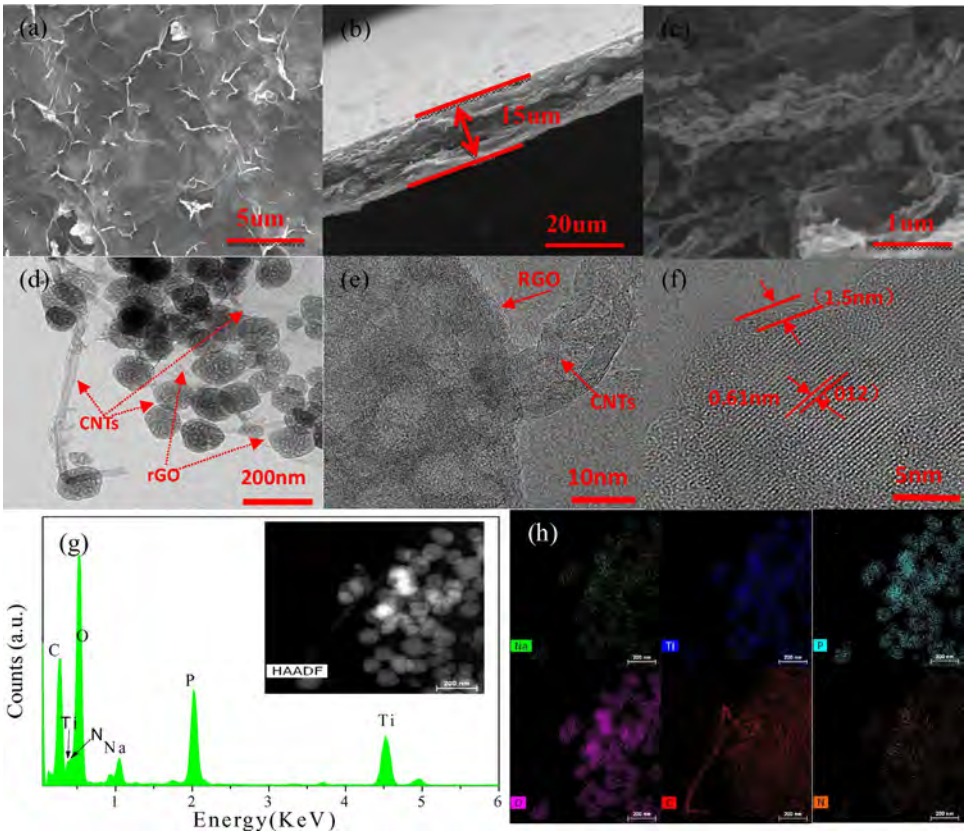

Fig. 2. (a)–(c) Representative SEM images of the monolithic C-MNTP⊂rGO-CNTs electrode; (d)-(f) Typical TEM and HR-TEM images of the monolithic C-MNTP⊂rGO-CNTs electrode; (g) and (h) EDS spectrum and TEM elemental maps of the monolithic C-MNTP⊂rGO-CNTs electrode. The inset in (e) shows the corresponding STEM image.

are negatively charged in water [29] and so when the CNTs/BSA-grafted MNTP hybrid and GO sheets are mixed in an aqueous solution, the electrostatic assembly leads to the formation of foam-like BSA-grafted MNTP⊂rGO-CNTs intermediate having a solid-like rheological behavior and sinking to the bottom (see Fig. 1). The foam-like BSA-grafted MNTP⊂rGO-CNTs intermediate is very stable and no MNTP nanocrystals precipitate even after several days, implying that the interconnected 3D GO networks without self-stacking are formed and the CNTs/BSA-grafted MNTP hybrids attach tightly to the GO sheets. Subsequent vacuum filtration and freeze drying produce the monolithic C-MNTP⊂rGO-CNTs intermediate with good mechanical integrity and it can be peeled off from the membrane since the building units of the BSA-grafted MNTP nanocrystals, CNTs, and GO are bound together by the strong interaction between the carboxylic (—COOH) and hydroxyl (–OH) groups. After annealing at 600 °C, the monolithic C-MNTP⊂rGO-CNTs assemblies are obtained accompanying reduction of GO to rGO and formation of ultrathin amorphous carbon layer on MNTP nanocrystals due to the carbonization of BSA. The amorphous carbon layer bridges the MNTP nanocrystals with CNTs and rGO to strengthen the internal structure, improve electron conduction, and prevent the monolithic C-MNTP⊂rGO-CNTs assemblies from disintegration. The porous structure with voids is created with the C-MNTP nanocrystals, CNTs, and rGO from carbonization of BSA and decomposition of the remaining NH_4HCO_3. As shown in Fig. 1, the monolithic C-MNTP⊂rGO-CNTs assemblies possess sufficient mechanical strength and toughness to maintain the self-supporting shape. At the same time, they have excellent flexibility and can be curved without fracturing (even 180° bending) making them suitable for flexible anodes in SIBs. The yield of the final product in such simple methodology is dependent on the mass of precursors and the volume of vacuum filtration device used during fabrication process, which is favorable for the mass production.

The morphology, structure, and composition of the monolithic C-MNTP⊂rGO-CNTs assemblies are characterized by SEM, TEM, XPS, XRD, TGA/DSC, Raman scattering and nitrogen adsorption–desorption isotherm measurements. The SEM images (Fig. 2a–c) reveal the self-supporting nature and outer surface along the in-plane direction. A layered structure with a uniform thickness about 15 μm is observed from the cross section SEM image (see Fig. 2b). The high-resolution SEM images in Fig. 2c show that segregated rGO sheets are interconnected with adjacent MNTP nanocrystals containing amorphous carbon on both sides of the former with abundant macroporous channels in the monolithic C-MNTP⊂rGO-CNTs assemblies. The results confirm that electrostatic interaction is effective in making the BSA-grafted MNTP nanocrystals settle preferentially at the functional group sites on the surface and periphery of the GO sheets, consequently suppressing self-stacking of GO and self-aggregation of the MNTP nanocrystals during hetero-assembly as well as inter-sheet stacking of rGO oriented to a directional flow during filtration [30]. No obvious CNTs aggregates are observed, revealing that the CNTs are distributed uniformly in the matrix and it is also confirmed by the top-view SEM images in Fig. 2a. The TEM images of the monolithic C-MNTP⊂rGO-CNTs assemblies show that the individual MNTP nanocrystals and their small aggregates are anchored on the rGO sheets and the CNTs as conductive species are dispersed in the surrounding MNTP nanocrystals and rGO sheets. The mesoporous characteristics of the MNTP nanocrystals and characteristic (012) lattice plane of the NASICON-type phase with a lattice spacing of 0.61 nm can be distinguished in the HR-TEM images in Figs. 2e and 2f, suggesting good structural conservation of the MNTP

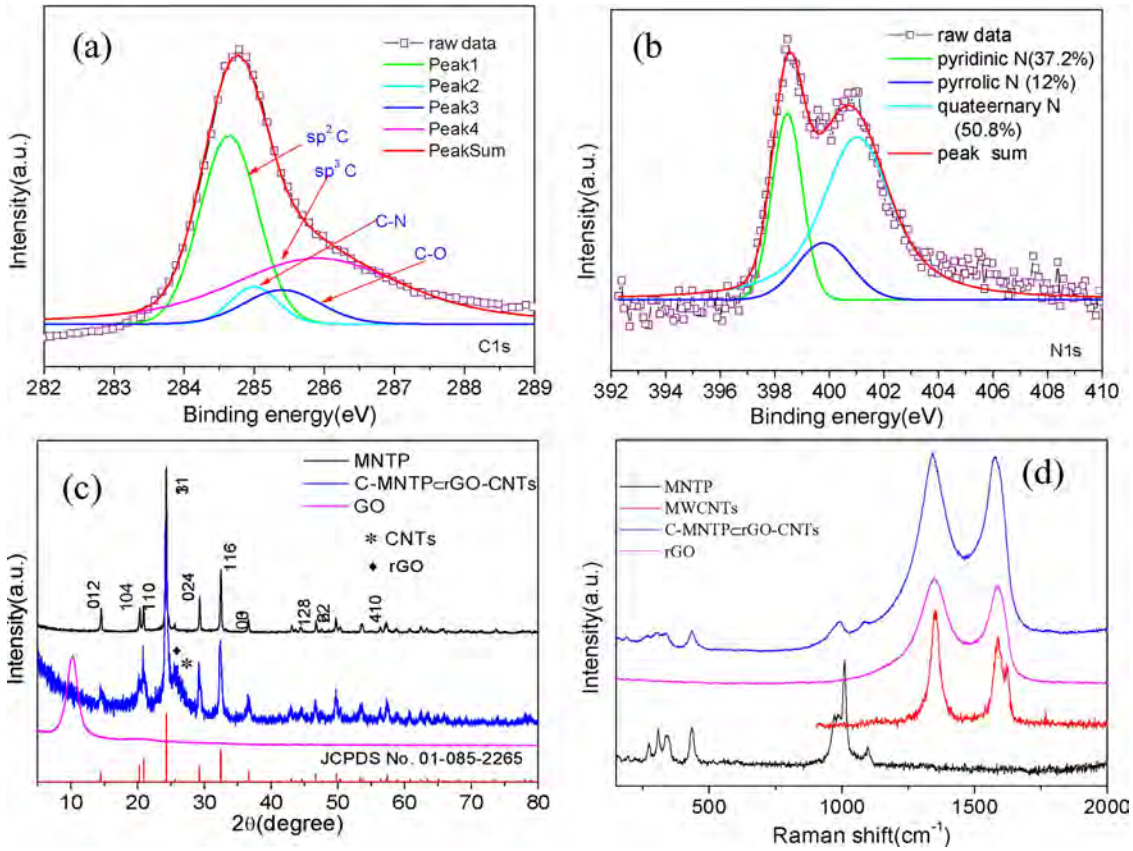

Fig. 3. (a) and (b) High-resolution C1s and N 1s spectra acquired from the monolithic C-MNTP⊂rGO-CNTs electrode; (c)-(d) XRD patterns and Raman scattering spectra of the monolithic C-MNTP⊂rGO-CNTs electrode and reference samples, respectively.

nanocrystals during the fabrication process. The high-resolution HR-TEM images disclose that a layer of 1.5 nm thick amorphous carbon on the MNTP nanocrystals acts as hinges to bridge the rGO sheets and CNTs. The STEM image (see the inset of Fig. 2g) confirms that the MNTP nanocrystals are intimately anchored to the rGO sheets with highly dispersed CNTs by the strong coupling interactions. The corresponding elemental maps (see Fig. 2h) indicate a homogeneous distribution of carbon in the monolithic C-MNTP⊂rGO-CNTs assemblies and obvious nitrogen doping in the amorphous carbon layer from carbonized BSA on the MNTP nanocrystals. For CNTs and rGO, according to TEM elemental maps, a relatively small amount of carbons have been substituted by nitrogen originated from the released nitrogen-containing functional group(for example, NH_4^+) from decomposed $(NH4)_2CO_3$ and BSA. The high-resolution XPS C1s spectrum (Fig. 3a) can be deconvoluted into a dominant component for *sp*2-C at 284.5 eV along with other weaker bands associated with *sp*3-C at 285.4 eV, C—N at 285.2 eV, and C—O at 285.9 eV. The N 1s peak can be observed from the XPS spectrum (Fig. S1) and the high-resolution N 1 s XPS spectrum (Fig. 3b) reveals three distinct N configurations with a peak area ratio of 3.1:1:5.9 corresponding to pyridinic N1 at 398.0 eV, pyrrolic (or pyridine) N2 at 399.3 eV, and quaternary (or graphitic) N3 at 400.7 eV, respectively. The large ratio of graphitic N3 will improve the electron conductivity as well as charge transfer at the interface between the C-MNTP and carbon network of rGO and CNTs, and also the electrochemical performance of the monolithic C-MNTP⊂rGO-CNTs assemblies as anodes in SIBs.

Fig. 3c depicts the XRD patterns which show that besides the peak at 26.4° associated with the CNTs and rGO, the other XRD peaks can be indexed to NASICON-type MNTP nanocrystals (JCPDS No. 01-085-2265) despite background noise due to relatively small weight of one self-supporting C-MNTP⊂rGO-CNTs assembly (about 20 mg). The intensity ratio of the first, second and third strongest peaks from MNTP nanocrystals in our sample is 1:0.49:0.38, which is comparable to the value (1:0.48:0.34)in standard JCPDS Card (No. 01-085-2265) for NTP. The small increment likely associates with unique mesoporous $NaTi_2(PO_4)_3$ nanocrystals, in which, larger numbers of (113) crystal plane are exposed to enhance corresponding peak intensity in XRD patterns. No obvious (002) peak located at 12.4° from GO is observed suggesting that GO has been reduced to rGO during the thermal treatment. The weak and broad characteristic diffraction peak from rGO and CNTs indicates that they are effectively separated without serious self-stacking and the C-MNTP nanocrystals are dispersed in the 3D rGO-CNTs matrix. Fig. 3d shows the Raman scattering spectra of the monolithic C-MNTP⊂rGO-CNTs assemblies and reference samples. The Raman bands at 990 and 1085 cm^{-1} are attributed to characteristic symmetrical and asymmetrical stretching in the NTP lattice. The peaks at 155 and 272 cm^{-1} originate from translational vibration of Ti^{4+} ions and those at 306, 341, and 438 cm^{-1} are associated with PO_4^{3-} [20]. Besides, two predominant peaks from amorphous carbon, rGO, and CNTs can be observed and can be assigned to the D band at approximately 1350 cm^{-1} derived from disordered carbon and the G band at about 1594 cm^{-1} associated with sp^2 hybridized carbon[31]. The Raman results confirm that the C-MNTP nanocrystals are well distributed in the 3D rGO-CNTs matrix. Fig. 4a shows the TGA/DSC results, revealing that the concentration of the MNTP nanocrystals in the monolithic C-MNTP⊂rGO-CNTs assemblies is 73 wt%. The mass loss of 22 wt% below 600 °C stems from decomposition of rGO and the amorphous carbon layer from the carbonization of BSA. The mass loss of 5 wt% observed between 600 and 700 °C stems from the CNTs. The specific surface area and porous structure of the monolithic C-MNTP⊂rGO-CNTs assemblies are evaluated by the nitrogen adsorption/desorption isotherms. Fig. 4b shows the characteristic type-IV hysteresis loop of mesoporous materials

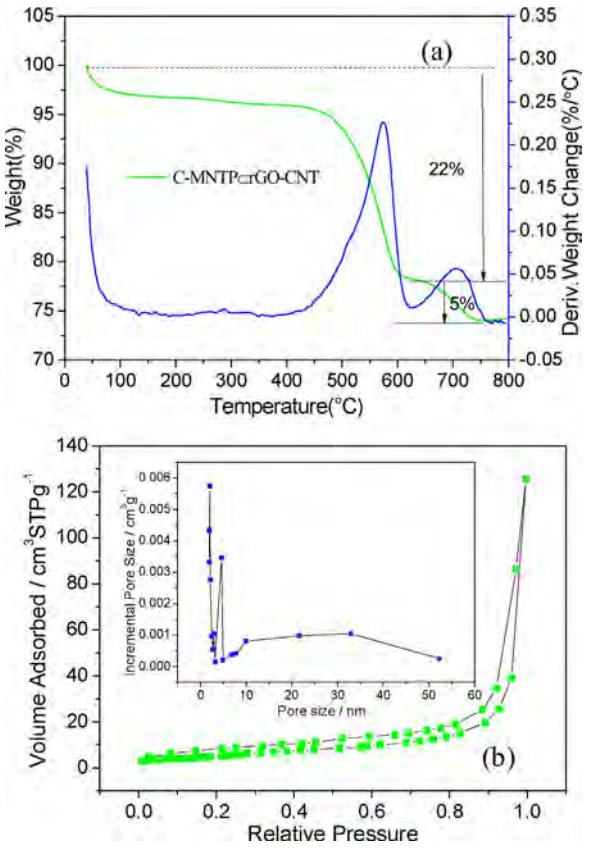

Fig. 4. (a) TGA/DSC curves and (b) Nitrogen-adsorption isotherms/corresponding pore-size distribution of the monolithic C-MNTP⊂rGO-CNTs electrode.

and surface area of 35.6 m^2/g. Based on the Barrett–Joyner–Halenda model, the sample possesses a broad pore size distribution between 1 and 50 nm (see inset in Fig. 4b). High incremental pore sizes at 4A are attributed to comprehensive effect of MNTP nanocrystals and surrounding carbon matrix. The results are similar with those in the composite comprising porous NTP nanocrystals embedded in a 3D graphene network [21]. The pore size distribution is different from those of pure MNTP nanocrystals (see Fig. S2), implying important influence of the surrounding carbon matrix. The hierarchical pores intertwined into micro-, meso-, and macro-pores with a large surface area of the monolithic C-MNTP⊂rGO-CNTs assemblies are desirable since it benefits charge transport and electrolyte diffusion into the dispersible MNTP nanocrystals to boost the Na storage performance [22,32].

The Na storage ability of the monolithic C-MNTP⊂rGO-CNTs assemblies is investigated in a voltage window between 1.5 and 3.0 V versus Na^+/Na in the coin-type cells with metallic Na foil as both the counter and reference electrodes. The discharge voltage of carbonaceous materials is below 1.0 V [15]. and hence, their contribution to the total capacity is small. The room-temperature (25 °C) Na storage behavior of the monolithic C-MNTP⊂rGO-CNTs electrode with a thickness of 15 μm is characterized by CV measurements using the initial five cycles at a scanning rate of 0.5 mV s^{-1}. As shown in Fig. 5a, a pair of well-defined reduction (~1.9 V)/oxidation (~2.3 V) peaks corresponding to the reversible Na^+ insertion–extraction reaction ($NaTi_2(PO_4)_3 + 2Na^+ + 2e^- \leftrightarrow Na_3Ti_2(PO_4)_3$) in the NTP lattice [12] is observed. The redox peak positions are unchanged during successive scans demonstrating outstanding reversibility of the monolithic C-MNTP⊂rGO-CNTs electrode. It is because hybridizing MNTP nanocrystals in the conductive and interconnected 3D hierarchical carbon matrix reduces the resistance in transporting

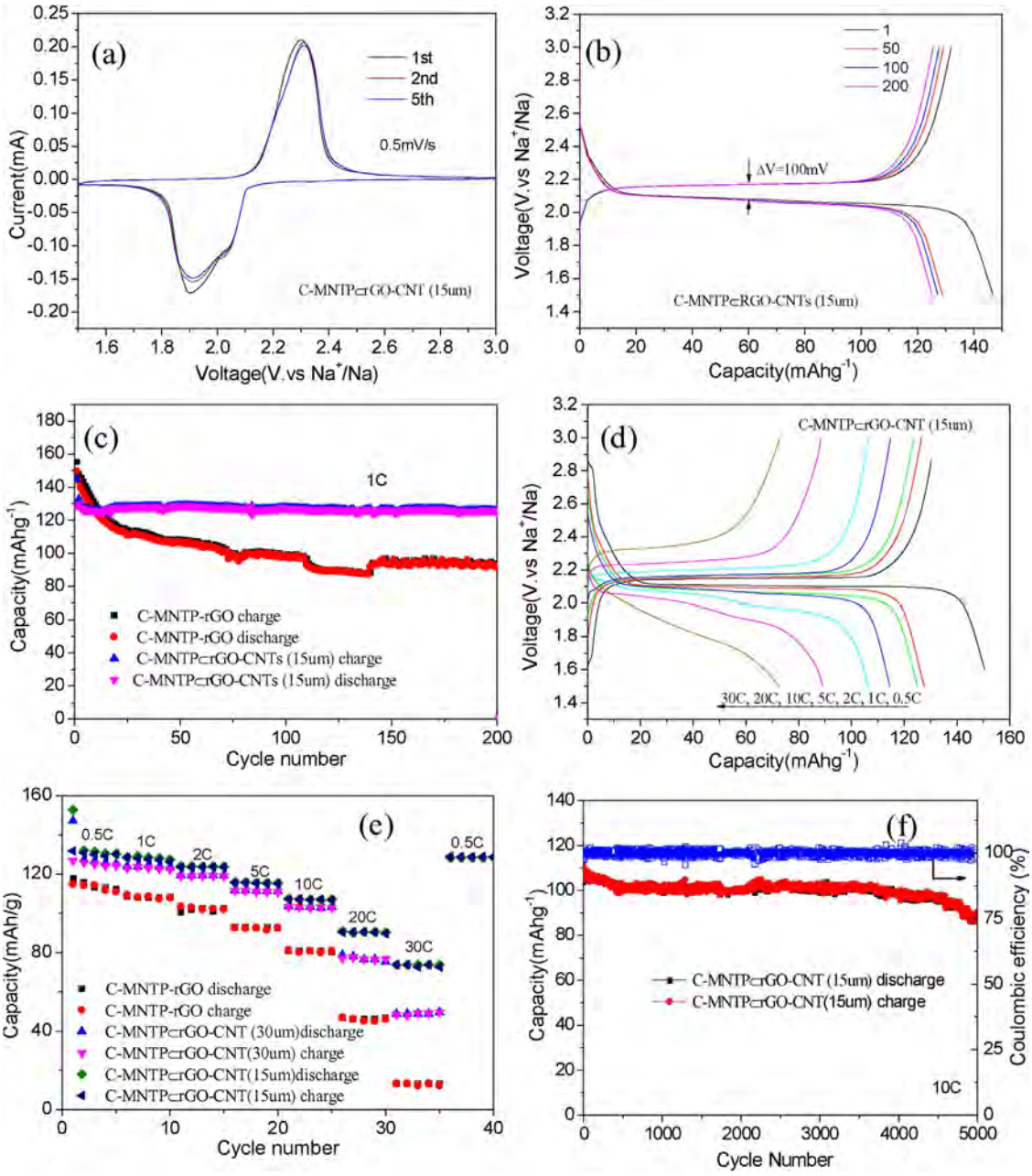

Fig. 5. (a) CV curves of the monolithic C-MNTP⊂rGO-CNTs electrode with a thickness of 15 μm for the initial three cycles at a scanning rate of 0.5 mVs^{-1}; (b) Typical GCD profiles of the monolithic C-MNTP⊂rGO-CNTs electrode with a thickness of 15 μm for the 1st, 50th, 100th, and 200th cycles at a current rate of 1 C; (c) Cycling performance of the monolithic C-MNTP⊂rGO-CNTs electrode with a thickness of 15 μm and the reference C-MNTP⊂rGO electrode at 1 C. (d) GCD profiles of the monolithic C-MNTP⊂rGO-CNTs electrode with a thickness of 15 μm at various current rates; (e) Rate performance and capacity retention of the monolithic C-MNTP⊂rGO-CNTs electrodes with different thicknesses and reference C-MNTP⊂rGO electrode; (f) Cycling performance and Coulombic efficiency of the monolithic C-MNTP⊂rGO-CNTs electrode with a thickness of 15 μm at 10 C;.

Na^+ ions and electrons. Fig. 5b shows the typical room-temperature GCD curves acquired from the monolithic C-MNTP⊂rGO-CNTs electrode at a current rate of 1 C (1 C = 133 $mAhg^{-1}$). They exhibit a well-defined and symmetrical flat voltage plateau at around 2.1 V corresponding to the redox reaction of Ti^{4+}/Ti^{3+}. The electrode shows small electrochemical polarization of 100 mV which is almost invariant with cycling. The results are different from those of the reference C-MNTP⊂rGO electrode that polarization increases gradually with cycling (Fig. S3). The low and stable electrochemical polarization of the monolithic C-MNTP⊂rGO-CNTs electrode implies high ion/electron conductivity as a result of the unique monolithic architecture of MNTP nanocrystals confined in the 3D hierarchical porous carbon framework. The initial discharging and charging capacities of the monolithic C-MNTP⊂rGO-CNTs electrode are 146 and 132 $mAhg^{-1}$, respectively, corresponding to a Coulombic efficiency (CE) of 90%. During cycling, the CE is improved to close to 99% indicating outstanding electrochemical reversibility. After 200 cycles at 1 C (Fig. 5c), the monolithic C-MNTP⊂rGO-CNTs electrode maintains a large reversible specific capacity of 126 $mAhg^{-1}$ and demonstrates outstanding cycling stability. The room-temperature cycling performance of the monolithic C-MNTP⊂rGO-CNTs assemblies is superior to that of the C-MNTP⊂rGO composite which exhibits large capacity fading with a reversible capacity of 92.4 $mAhg^{-1}$ after 200 cycles. Hence, combining the conductive carbon nanotubes with the monolithic assemblies creates robust and well-

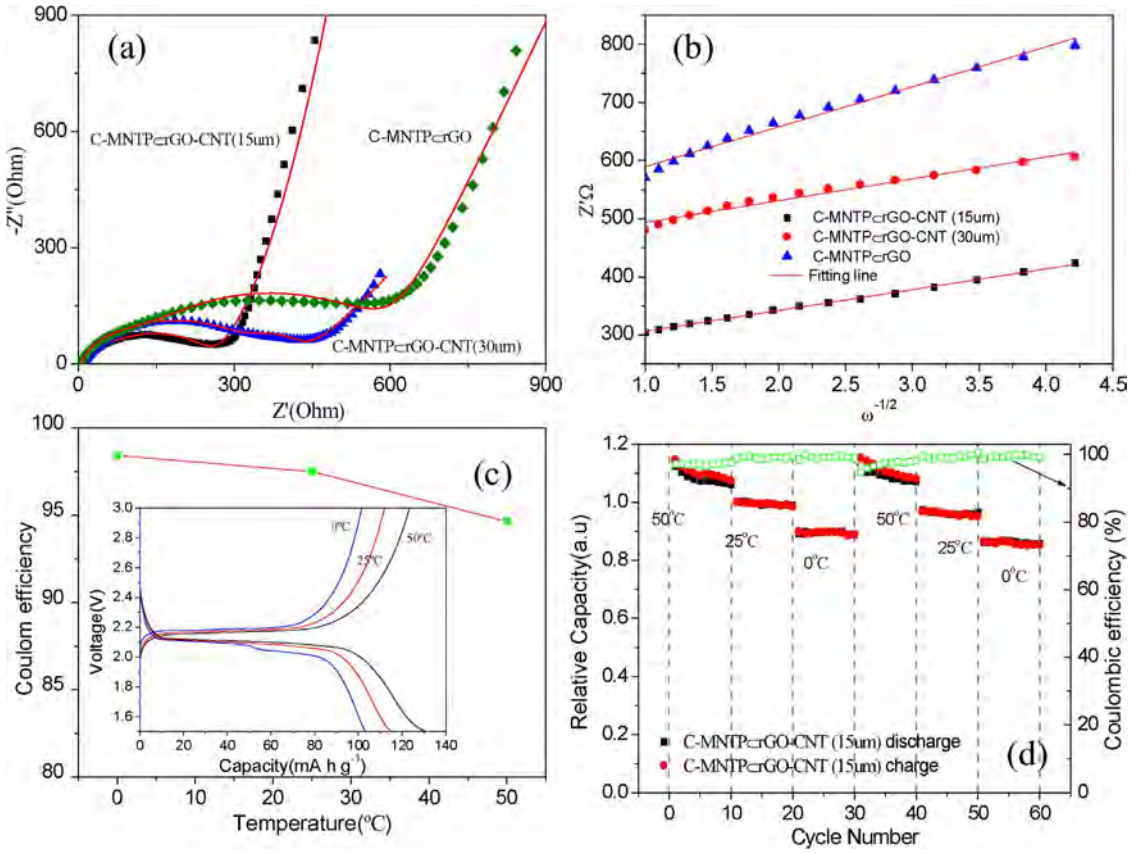

Fig. 6. (a) Nyquist plots of the C-MNTP⊂rGO, C-MNTP⊂rGO-CNTs (15 μm) and C-MNTP⊂rGO-CNTs (30 μm) electrodes after the rate capability test; (b) Corresponding Z' plots against $\varpi^{-1/2}$ in the low frequency region (10–0.1 Hz); (c) Initial Coulombic efficiency and GCD profiles (inset) of the monolithic C-MNTP⊂rGO-CNTs electrode with a thickness of 15 μm at 1 C at different temperature of 0, 25 and 50 °C; (d) Corresponding cycling performance at 0, 25, and 50 °C.

interconnected conductive pathways in the electrode matrix to provide excellent current-collecting networks for electron transport. The room-temperature GCD profiles acquired at different current densities from 0.5 to 30 C (Fig. 5d) of the monolithic C-MNTP⊂rGO-CNTs electrode with a thickness of 15 μm show a well-defined and symmetrical flat voltage plateau in spite of perceptible polarization at the high current density of 30 C indicative of better rate capability. The corresponding rate performance (Fig. 5e) shows high and stable capacity. At rates of 0.5, 1, 2, 5, 10, and 20 C, the monolithic C-MNTP⊂rGO-CNTs electrode with a thickness of 15 μm delivers discharge capacities of 132, 128, 123, 116, 107, and 90 mAhg^{-1}, respectively. Even at 50 C, a reversible capacity of 73 mAhg^{-1} is maintained implying rapid charging and discharging within a few minutes for high energy and power densities. When the rate is returned to 0.5 C after high-rate cycling, a high capacity of 127 mAh g^{-1} in subsequent cycling can be recovered, suggesting good structural integrity of the prepared electrode. By comparison, the discharge capacities of MNTP in traditional electrode (see Fig. S4) and self-supporting C-MNTP⊂rGO electrode are lower at various rates. More importantly, the monolithic C-MNTP⊂rGO-CNTs electrode with a thickness of 30 μm or twice the areal mass loading still delivers competitive rate performance with a capacity of 49 mAh g^{-1} at a rate of 30 C. In contrast, the reference C-MNTP⊂rGO anode delivers a poor rate-performance with a capacity of only 45 mAhg^{-1} at 20 C. In particular, the relative increase in the discharge capacity of the monolithic C-MNTP⊂rGO-CNTs electrode is larger at higher rates, implying fast Na^+ diffusion and high reversible electrochemical reactions due to the formation of robust and well-interconnected conductive networks in the electrode after carbon nanotubes are introduced. The monolithic C-MNTP⊂rGO-CNTs electrode delivers outstanding long-cycling performance at high rates. As shown in Fig. 5e, the electrode with a thickness of 15 μm at a rate of 10 C shows a reversible capacity of 107 mAhg^{-1} in the first cycle and a capacity of 88 mAhg^{-1} is retained after 5,000 cycles with only 0.0036% loss per cycle and high Coulombic efficiency of 98%. To the best of our knowledge, the high-rate and long cycle-life performance have not been achieved from flexible and monolithic NTP anodes for Na storage. The performance from monolithic C-MNTP⊂rGO-CNTs electrode is also comparable to those NTP-based electrodes (see Table SI) produced by the traditional slurry-coating process such as h-MNTP/MWCNTs [26] and self-supporting C-MNTP⊂CNTs electrodes (see Fig. S4). The morphology and crystalline structure of the monolithic C-MNTP⊂rGO-CNTs electrode after cycling are studied by SEM and Raman scattering. Even after 5,000 cycles at 10C, the original quasi-spherical morphology of the MNTP nanocrystals is preserved (Fig. S5) and the characteristic Raman peaks from the NASICON-type NTP nanocrystals can be identified (Fig. S4), suggesting robust structural stability. To investigate the reason for the excellent Na storage performance, EIS is carried out after the rate capability test. The Nyquist plots (Fig. 6a) show a semicircle in the high-middle frequency range and straight line in low frequency region. The semicircle represents charge transfer resistance (Rct) between the

Table 1
R_s, R_e, R_{ct}, б and D_i of for the C-MNTP⊂rGO-CNTs electrodes and reference sample after rate tests using the half-cells according to Fig. 6a and b.

Samples	$R_s(\Omega)$	$R_e(\Omega)$	$R_{ct}(\Omega)$	б	$D_{Na}(cm^2s^{-1})$
C-MNTP⊂rGO-CNTs(15um)	4.569	40.1	200.5	36	$5.2*10^{-13}$
C-MNTP⊂rGO-CNTs(30um)	5.245	56.9	334.1	39	$3.4*10^{-13}$
C-MNTP⊂RGO	5.896	68.6	456.3	72	$1.4*10^{-14}$

electrolyte and electrode. Based on the equivalent circuit model in Fig. S6, R_{ct} (Table 1) of the monolithic C-MNTP⊂rGO-CNTs electrodes is smaller than that of the reference C-MNTP⊂rGO electrode. It indicates that combining the highly conductive carbon nanotubes with a monolithic hierarchical electrode reduces polarization leading to efficient charge transport between the MNTP nanocrystals and electrolyte during the electrochemical reaction. The Na^+ chemical diffusion coefficient (D_{Na}) are calculated according to the following equations [33,34]:

$$D_{Na}=\frac{R^2T^2}{2A^2n^4F^4C^2\sigma^2} \quad (1)$$

$$Z' = R_s + R_{ct} + \sigma\omega^{-1/2} \quad (2)$$

where *R, T,A, n, F, C and* σ are the gas constant, absolute temperature, surface area of the electrode, number of electrons transferred in the half reaction of the redox couple, Faraday's constant, Na^+ concentration, and Warburg factor, respectively. The value of σ can be obtained (Table 1) from the slope of the lines between Z' and $\varpi^{-1/2}$ shown in Fig. 6b. The calculated D_{Na} values of the monolithic C-MNTP⊂rGO-CNTs electrodes (Table 1) are larger than that of the reference C-MNTP⊂rGO electrode, suggesting that highly conductive carbon nanotubes suppress re-stacking of the rGO sheets, enabling fast migration of Na^+ to the interior of MNTP nanocrystals since they are linked by inter-connected hierarchical porous carbon matrix.

The aforementioned outstanding performance can be attributed to the following factors. Firstly, the interstitial mesoporous framework from the MNTP nanocrystals provides short ion diffusion lengths and abundant active sites for Na^+ intercalation. Secondly, the ultrathin N doped amorphous carbon layers act as an effective "hinge" to bridge the MNTP nanocrystals with the 3D interconnected networks of rGO and CNTs and enhance electroactive surface area of MNTP nanocrystals for full utilization during electrochemical reaction [35]; whereas incorporation of CNTs provides robust and interconnected conductive pathways in the electrode matrix leading to close contact between the MNTP nanocrystals and the surrounding carbon matrix for rapid electron transport in the electrode. Thirdly, the hierarchical porous structure in the monolithic C-MNTP⊂rGO-CNTs electrode not only facilitates electrolyte accessibility to ensure effective Na^+ supply for the electrochemical reaction, but also prevents self-aggregation among the MNTP nanocrystals and helps to buffer the strain effects caused by the volume change during Na insertion/extraction. This ensures effective electrical contact between the MNTP nanocrystals and surrounding carbon matrix during cycling and introduces mechanical and chemical robustness to the electrode. In particular, the CNTs suppress re-stacking of the rGO sheets and provide highly conductive pathways for electron and ion transport and better mechanical properties than a single component, so that the Na storage ability is improved. In addition to the high capacity, high-rate capability, and long cycle life, it is desirable to produce a battery that operates in a wide temperature range [36,37]. The inset in Fig. 6c compares the initial charging and discharging curves of the C-MNTP⊂rGO-CNTs electrode at a current rate of 1C at 0 °C (Fig. S7), 25 °C (RT), and 50 °C (Fig. S6). When the temperature is 0 °C, the charging and discharging capacities diminish, but the Coulombic efficiency increases to nearly 99% (Fig. 6c). The smaller capacities are attributed to the degraded conductivity of the electrolyte at 0 °C. Interesting, the well-defined step (plateau splitting) appears in the discharge voltage profile of the C-MNTP⊂rGO-CNTs electrode at 0 °C. This phenomenon was often observed in NASICON compound as anodes, for example, $NaTi_2(PO_4)_3$ at low temperatures [38] and $Na_3V_2(PO_4)_3$ at higher current rates [39]. Although the underlying physical origin remains ambiguous, it probably associates with the transfer of Na ions between the 6-coordinate and 8-coordinate sites due to the change of temperature [40]. This rearrangement triggers a number of small but significant changes in the NASICON framework, thereby inducing plateau splitting in the discharge voltage profile. When the temperature is raised to 25 °C, the capacities recover to the RT values at a current rate of 1C with Coulombic efficiency higher than 98% (Fig. 6d). When the temperature is further raised to 50 °C, the relative discharging capacity of the C-MNTP⊂rGO-CNTs electrode increases at a current rate of 1C but the Coulombic efficiency becomes worse (Fig. 6d). In general, the diffusion and irregular movement of ions are accelerated with temperature increment. Simultaneously ion scattering with surrounding lattice increases at elevated temperature. This enhanced inelastic scattering due to the increased temperature will lead to electric energy loss, thereby depressing Coulombic efficiency. This phenomenon has recently observed in free-standing GNHPG foam as a cathode for rechargeable Al-ion batteries [37]. We consider that this explanation is also applicable to our observed results. It should be pointed out that when the temperature is reduced to 25 °C, the discharging capacities recover to the RT values at a current rate of 1C and the increased Coulombic efficiency is larger than 98%. The results reveal the advantages of the monolithic hierarchical carbon assemblies embedded with MNTP nanocrystals suggesting large potential in flexible high-performance sodium anodes in energy storage applications.

4. Conclusion

Two-step hetero-assembly induced by electrostatic interaction is exploited to fabricate flexible and monolithic hierarchical porous assemblies consisting of rGO sheets, CNTs, and 73 wt% MNTP nanocrystals with ultrathin amorphous N-doped carbon layers. The materials are synthesized by vacuum filtration and annealing. In the nanocomposite, the ultrathin amorphous carbon layers become effective hinges to connect MNTP nanocrystals with the 3D interconnected networks of rGO and CNTs. Incorporation of CNTs into the monolithic assemblies suppresses re-stacking of rGO sheets, provides robust and interconnected conductive pathways in the electrode matrix to facilitate charge transfer, enhances the reaction kinetics, and ensures better mechanical properties compared to a single component. The flexible and monolithic C-MNTP⊂rGO-CNTs assemblies as anodes for SIBs deliver outstanding RT electrochemical performance with a large reversible capacity (125 $mAhg^{-1}$ at 1 C), long cycling life (82% capacity retention after 5,000 cycles at 10 C), and high rate capability (73 $mAhg^{-1}$ at 30 C). At 0 and 50 °C, the flexible monolithic anode delivers competitive performance such as high Coulombic efficiency and reversible capacity. Our results suggest a simple and efficient method to produce flexible and monolithic nanocomposite membranes in high-performance anodes for SIBs to power portable, flexible, and wearable electronics.

Acknowledgements

This work was financially supported by the Grants from the National Natural Science Foundation of China (Nos. 11474242, 51472209 and U1401241), Hunan Provincial Innovation Foundation for Graduate (No.CX2016B254), and City University of Hong Kong Applied Research Grant (ARG) No. 9667122.

Appendix A. Supplementary data

Supplementary data associated with this article can be found, in the online version, at http://dx.doi.org/10.1016/j.electacta.2017.09.121.

References

[1] W. Liu, M.-S. Song, B. Kong, Y. Cui, Advanced Materials 29 (2017) 1603436.
[2] H. Wu, Y. Huang, F. Xu, Y. Duan, Z. Yin, Advanced Materials 28 (2016) 9881–9919.
[3] L. Wen, F. Li, H.M. Cheng, Advanced Materials 28 (2016) 4306–4337.
[4] G. Xu, L. Yang, X. Wei, J. Ding, J. Zhong, P.K. Chu, Advanced Functional Materials 26 (2016) 3349–3358.
[5] C. Zhu, P. Kopold, P.A. van Aken, J. Maier, Y. Yu, Advanced Materials 28 (2016) 2409–2416.
[6] H. Hou, X. Qiu, W. Wei, Y. Zhang, X. Ji, Advanced Energy Materials (2017), doi: http://dx.doi.org/10.1002/aenm.201602898.
[7] H. Hou, C.E. Banks, M. Jing, Y. Zhang, X. Ji, Advanced Materials 27 (2015) 7861–7866.
[8] C.P. Grey, J.M. Tarascon, Nat Mater 16 (2017) 45–56.
[9] J. Lu, Z. Chen, Z. Ma, F. Pan, L.A. Curtiss, K. Amine, Nat Nano 11 (2016) 1031–1038.
[10] Z. Jian, Y.-S. Hu, X. Ji, W. Chen, Advanced Materials (2017), doi:http://dx.doi.org/10.1002/adma.201601925.
[11] Z. Li, D. Young, K. Xiang, W.C. Carter, Y.M. Chiang, Advanced Energy Materials 3 (2013) 290–294.
[12] S.I. Park, I. Gocheva, S. Okada, J.-i. Yamaki, Journal of The Electrochemical Society 158 (2011) A1067–A1070.
[13] G. Pang, P. Nie, C. Yuan, L. Shen, X. Zhang, H. Li, C. Zhang, Journal of Materials Chemistry A 2 (2014) 20659–20666.
[14] G. Pang, C. Yuan, P. Nie, B. Ding, J. Zhu, X. Zhang, Nanoscale 6 (2014) 6328–6334.
[15] C. Xu, Y. Xu, C. Tang, Q. Wei, J. Meng, L. Huang, L. Zhou, G. Zhang, L. He, L. Mai, Nano Energy 28 (2016) 224–231.
[16] G. Yang, H. Song, M. Wu, C. Wang, Journal of Materials Chemistry A 3 (2015) 18718–18726.
[17] J. Yang, H. Wang, P. Hu, J. Qi, L. Guo, L. Wang, Small 11 (2015) 3744–3749.
[18] B. Zhao, B. Lin, S. Zhang, C. Deng, Nanoscale 7 (2015) 18552–18560.
[19] B. Zhao, Q. Wang, S. Zhang, C. Deng, Journal of Materials Chemistry A 3 (2015) 12089–12096.
[20] H.-K. Roh, H.-K. Kim, M.-S. Kim, D.-H. Kim, K.Y. Chung, K.C. Roh, K.-B. Kim, Nano Research 9 (2016) 1844–1855.
[21] C. Wu, P. Kopold, Y.-L. Ding, P.A. van Aken, J. Maier, Y. Yu, ACS nano 9 (2015) 6610–6618.
[22] Y. Fang, L. Xiao, J. Qian, Y. Cao, X. Ai, Y. Huang, H. Yang, Advanced Energy Materials 6 (2016) n/a-n/a.
[23] G. Xu, L. Yang, Z. Li, X. Wei, P.K. Chu, Journal of Materials Chemistry A 5 (2017) 2749–2758.
[24] Y. Fang, L. Xiao, X. Ai, Y. Cao, H. Yang, Advanced Materials 27 (2015) 5895–5900.
[25] G. Pang, C. Yuan, P. Nie, J. Zhu, X. Zhang, H. Li, B. Ding, Applied Materials Today 4 (2016) 54–61.
[26] G.B. Xu, L.W. Yang, X.L. Wei, J.W. Ding, J.X. Zhong, P.K. Chu, Journal of Power Sources 327 (2016) 580–590.
[27] G. Xu, Y. Tian, X. Wei, L. Yang, P.K. Chu, Journal of Power Sources 337 (2017) 180–188.
[28] Y.J. Yun, W.G. Hong, W.-J. Kim, Y. Jun, B.H. Kim, Advanced Materials 25 (2013) 5701–5705.
[29] J. Rong, M. Ge, X. Fang, C. Zhou, Nano letters 14 (2013) 473–479.
[30] M. Zhou, X. Li, B. Wang, Y. Zhang, J. Ning, Z. Xiao, X. Zhang, Y. Chang, L. Zhi, Nano letters 15 (2015) 6222–6228.
[31] A.M. Rao, A. Jorio, M.A. Pimenta, M.S.S. Dantas, R. Saito, G. Dresselhaus, M.S. Dresselhaus, Physical Review Letters 84 (2000) 1820–1823.
[32] Y. Liu, X. He, D. Hanlon, A. Harvey, J.N. Coleman, Y. Li, ACS Nano 10 (2016) 8821–8828.
[33] C. Han, Y. He, B. Li, H. Li, J. Ma, H. Du, X. Qin, Q. Yang, F. Kang, ChemSusChem 7 (2014) 2567–2574.
[34] G. Xu, L. Yang, X. Wei, J. Ding, J. Zhong, P. Chu, Journal of Power Sources 295 (2015) 305–313.
[35] M. Krajewski, B. Hamankiewicz, A. Czerwiński, Electrochimica Acta 219 (2016) 277–283.
[36] G. Zhu, K. Wen, W. Lv, X. Zhou, Y. Liang, F. Yang, Z. Chen, M. Zou, J. Li, Y. Zhang, W. He, Journal of Power Sources 300 (2015) 29–40.
[37] X. Yu, B. Wang, D. Gong, Z. Xu, B. Lu, Advanced Materials 29 (2017) 1604118.
[38] L. Wang, B. Wang, G. Liu, T. Liu, T. Gao, D. Wang, RSC Advances 6 (2016) 70277–70283.
[39] K. Saravanan, C.W. Mason, A. Rudola, K.H. Wong, P. Balaya, Advanced Energy Materials 3 (2013) 444–450.
[40] C. Masquelier, C. Wurm, J. Rodriguez-Carvajal, J. Gaubicher, L. Nazar, Chemistry of Materials 12 (2000) 525–532.

Supporting Information

Monolithic Hierarchical Carbon Assemblies Embedded with Mesoporous $NaTi_2(PO_4)_3$ Nanocrystals for Flexible High-Performance Sodium Anodes

Guobao Xu[a], Zhongyu Li[a], Xiaolin Wei[a], Liwen Yang[a*], Paul K Chu[b]

[a] *Hunan Key Laboratory of Micro-Nano Energy Materials and Devices, School of Physics and Optoelectronics, Xiangtan University, Hunan 411105, China*

[b] *Department of Physics and Materials Science, City University of Hong Kong, Tat Chee Avenue, Kowloon, Hong Kong, China*

[*] Corresponding authors: ylwxtu@xtu.edu.cn (L.W. Yang)

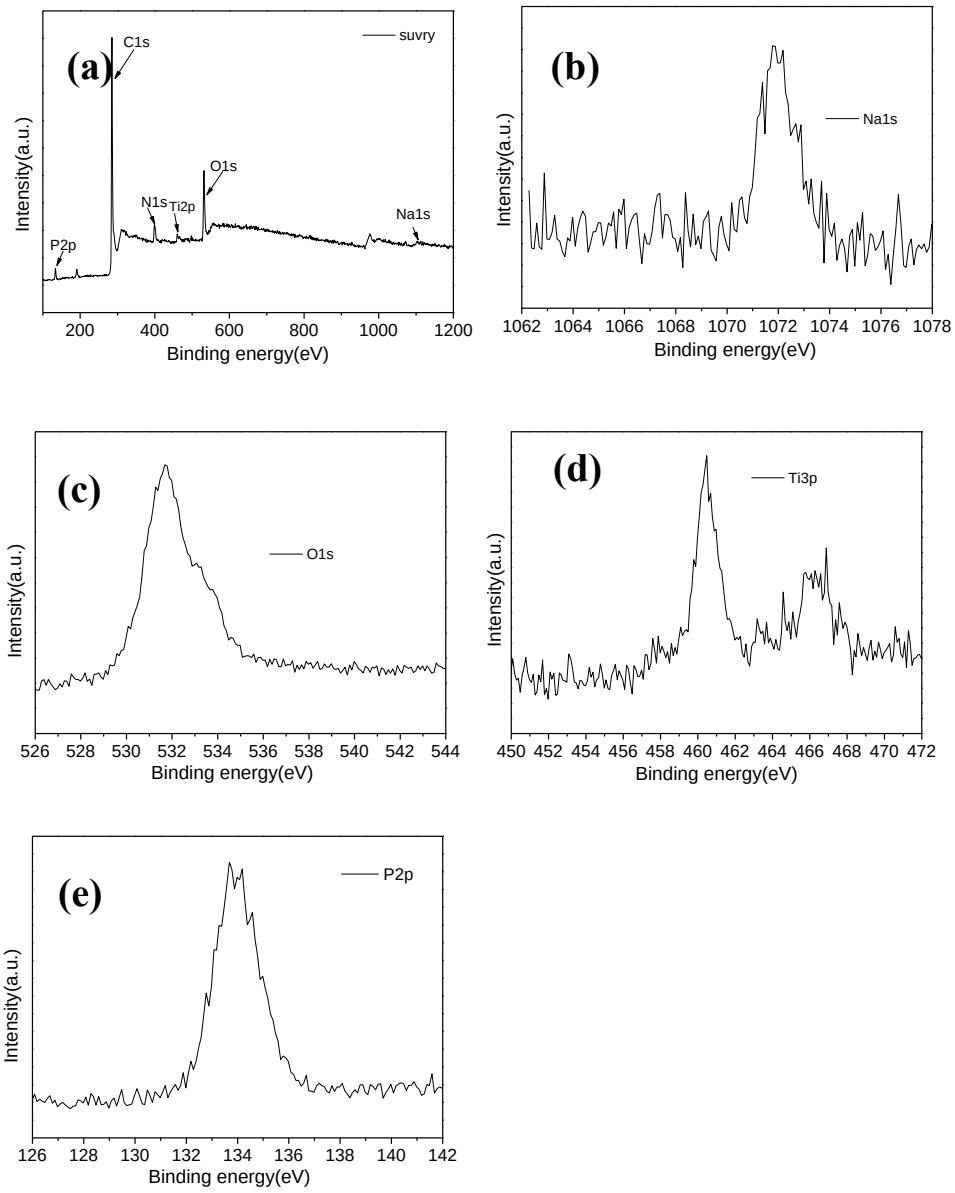

Figure S1. XPS spectra of the C-MNTP⊂rGO-CNTs assemblies (a) Survey spectrum and (b-e) High-resolution Na 1s, O 1s, Ti 3p, and P2p spectra.

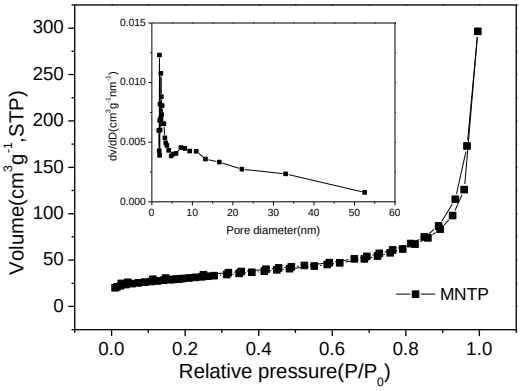

Figure S2 Nitrogen adsorption–desorption isotherms and corresponding pore size distribution(see inset) of the MNTP NCs.

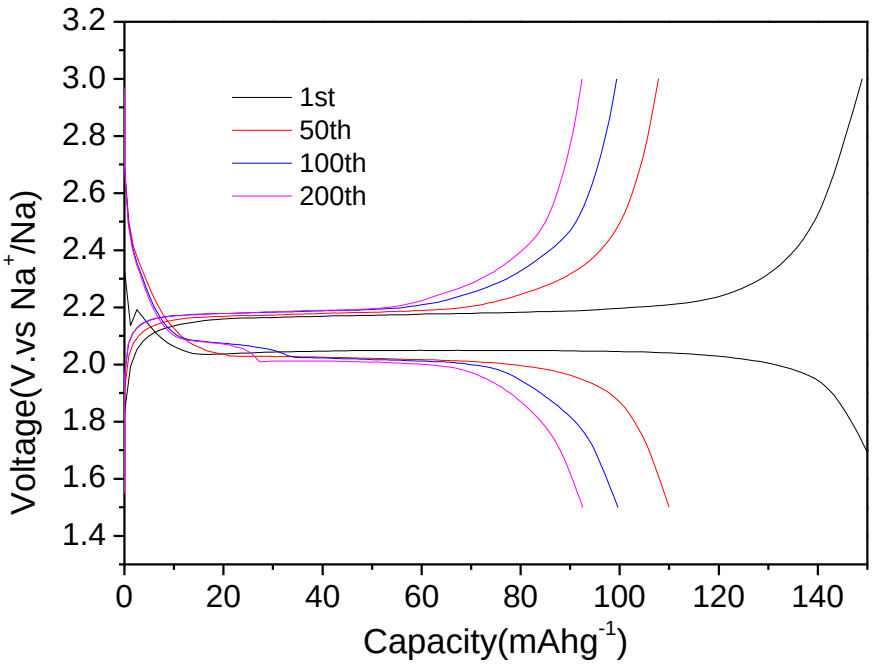

Figure S3. Discharge-charge profiles of the C-MNTP⊂rGO electrode at 1 C.

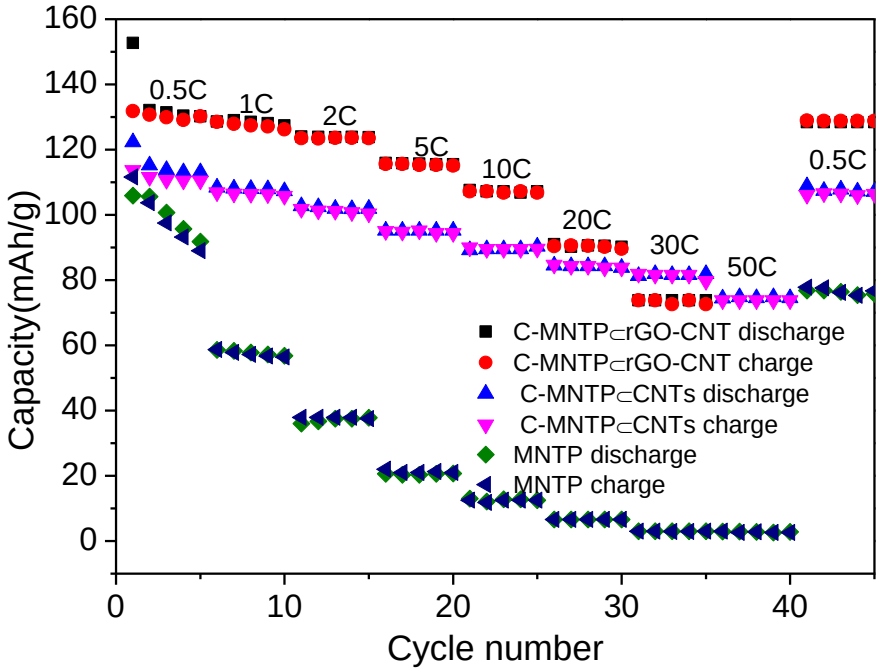

Figure S4. Rate performance and capacity retention of the C-MNTP⊂rGO-CNT, C-MNTP⊂CNTs and MNTP electrodes

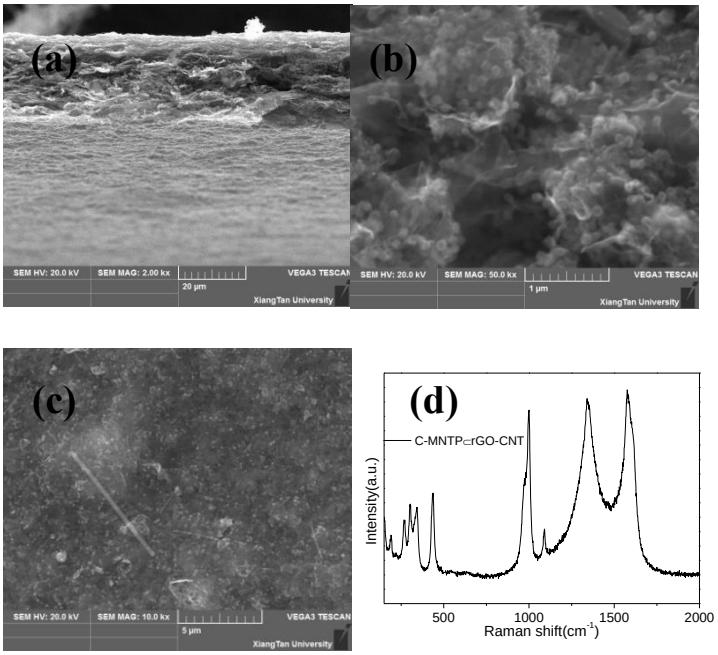

Figure S5. (a-c) Representative SEM images of the C-MNTP⊂rGO-CNTs electrode after 5,000 cycles at 10C and (d) Corresponding Raman scattering spectrum.

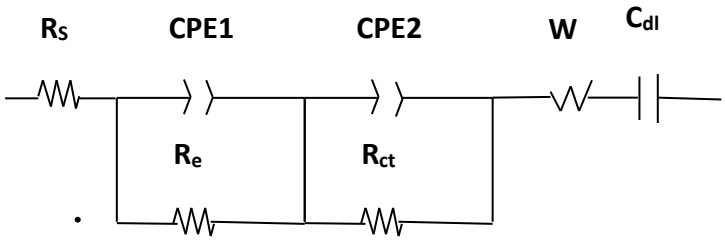

Figure S6. Equivalent circuit used to fit the EIS data in Figure 6a. R_{ct} stands for the charge transfer resistance and the other components R_s, CPE, R_e, W, and C_{dl} represent the total resistance of the electrolyte, constant phase-angle element, diffusion resistance of Na ions through the interface, Warburg impedance, and double layer capacitance, respectively.

Electric heating sleeve Mixture of ice and water

Figure S7. (a) and (b) Digital photographs showing the apparatus to determine the electrochemical performance of the C-MNTP⊂rGO-CNTs electrode at 0, 25 (room temperature), and 50 ^{o}C.

Table SI. High rate performance and cycling performance of typical $NaTi_2(PO_4)_3$-based composites prepared by different methods.

Compounds	10 C capacity [$mAhg^{-1}$]	30 C capacity [$mAhg^{-1}$]	Capacity retention at 10 C	References
C-MNTP⊂rGO-CNTs	**107**	**73**	**82.3% over 5000 cycles**	**This work**
Porous $NaTi_2(PO_4)_3$ Embedded in 3D Graphene Networks	106	67(50C)	80% over 1000 cycles	**[1]**
3D Graphene Decorated $NaTi_2(PO_4)_3$ Microspheres	122	118	77% over 1000 cycles(20C)	**[2]**
$NaTi_2(PO_4)_3$/rGO composite	95(9.2C)	78(36.8C)	85% over 150 cycles(1C)	[3]
$NaTi_2(PO_4)_3$/rGO 2D nanocomposite	112	105	95.5% over 1000 cycles	[4]
$NaTi_2(PO_4)_3$/CMK-3 nanohybrid	101(0.2C)	39(2C)	81.8% over 1000 cycles	[5]
$NaTi_2(PO_4)_3$Nanocubes	83.5	77.2(20C)	89.3% over 10000	[6]

with Synergistic Coating of Carbon and Rutile TiO_2			cycles	
Carbon-Coated Hierarchical $NaTi_2(PO_4)_3$ Mesoporous Microflowers	111	102	77.3% over 10000cycles(20C)	[7]
$NaTi_2(PO_4)_3$–graphene nanocomposite	65	40(40C)	90% over 100 cycles(2C)	[8]
NaTi2(PO4)3/C porous plates	85	85(10C)	82.4% over 120 cycles (10C)	[9]
Carbon Coated $NaTi_2(PO_4)_3$	124	120 （40C）	72.8% over 6000 cycles(50C)	[10]
h-MNTP/MWCNTs composite	106	82	76% over 2000 cycles(10C)	[11]

References

[1] C. Wu, P. Kopold, Y.-L. Ding, P.A. van Aken, J. Maier, Y. Yu, ACS nano 9 (2015) 6610-6618.

[2] Y. Fang, L. Xiao, J. Qian, Y. Cao, X. Ai, Y. Huang, H. Yang, Advanced Energy Materials 6 (2016).

[3] J. Song, S. Park, J. Gim, V. Mathew, S. Kim, J. Jo, S. Kim, J. Kim, Journal of Materials Chemistry A 4 (2016) 7815-7822.

[4] H.-K. Roh, H.-K. Kim, M.-S. Kim, D.-H. Kim, K.Y. Chung, K.C. Roh, K.-B. Kim, Nano Research 9 (2016) 1844-1855.

[5] G. Pang, P. Nie, C. Yuan, L. Shen, X. Zhang, H. Li, C. Zhang, Journal of Materials Chemistry A 2 (2014) 20659-20666.

[6] J. Yang, H. Wang, P. Hu, J. Qi, L. Guo, L. Wang, Small 11 (2015) 3744-3749.

[7] C. Xu, Y. Xu, C. Tang, Q. Wei, J. Meng, L. Huang, L. Zhou, G. Zhang, L. He, L. Mai, Nano Energy 28 (2016) 224-231.

[8] G. Pang, C. Yuan, P. Nie, B. Ding, J. Zhu, X. Zhang, Nanoscale 6 (2014) 6328-6334.

[9] Z. Huang, L. Liu, L. Yi, W. Xiao, M. Li, Q. Zhou, G. Guo, X. Chen, H. Shu, X. Yang, Journal of Power Sources 325 (2016) 474-481.

[10] Y. Jiang, J. Shi, M. Wang, L. Zeng, L. Gu, Y. Yu, ACS applied materials & interfaces 8 (2015) 689-695.

[11] G.B. Xu, L.W. Yang, X.L. Wei, J.W. Ding, J.X. Zhong, P.K. Chu, Journal of Power Sources 327 (2016) 580-590.